Rod-like amphiphilic AIE-active NIR probe enables super-early precise in-vivo detection of Aβ fibrils/plaques

Yipu Wang
East China University of Science and Technology
Dong Mei
Clinical Research Center, Beijing Children's Hospital, Capital Medical University, National Center for Children's Health
Xinyi Zhang
East China University of Science and Technology
Da-Hui Qu
East China University of Science and Technology https://orcid.org/0000-0002-2039-3564
Ju Mei (daisymeiju@ecust.edu.cn)
East China University of Science and Technology https://orcid.org/0000-0001-9992-8877
He Tian
East China University of Science and Technology https://orcid.org/0000-0003-3547-7485

Article

Keywords: Aβ fibrils/plaques, Alzheimer's disease (AD), proteins, diagnosis

Posted Date: May 10th, 2021

DOI: https://doi.org/10.21203/rs.3.rs-232117/v1

Abstract

Precise and early detection of Aβ fibrils/plaques is pivotal to the diagnosis and treatment of Alzheimer's disease (AD), a serious disease threatening human health. Optical imaging stands out to be a promising technique for such task. However, restricted by poor blood-brain barrier penetrability, short-wavelength excitation and emission, and aggregation-caused quenching effect, the clinically used gold-standard probes are usually powerless in early *in-vivo* diagnosis of AD. To address these issues, we put forward an “all-in-one” design principle and develop a simple rod-like amphiphilic NIR AIE probe to demonstrate its feasibility. *In-vitro*, *ex-vivo*, and *in-vivo* experiments with different strains of mice indicates that AIE-CNPy-AD holds the universality to Aβ fibrils/plaques identification. Noteworthily, AIE-CNPy-AD is even able to precisely trace the small and sparsely-distributed Aβ fibrils/plaques in AD model mice as young as 4-month-old APP/PS1 mice, the youngest having Aβ deposits, suggesting the probe might be an ideal alternative for early AD diagnosis.

Introduction

Alzheimer's disease (AD) is a degenerative disease of the nervous system, which will lead to memory loss, behavior disorder, cognitive decline, and eventually death[1-3]. According to the statistic, there are about 50 million patients with Alzheimer's disease all over the world. It is predicted that the number of AD patients will increase to 150 million by 2050, exerting serious social and economic burden to countries worldwide[4,5]. Currently, clinical diagnosis of AD patients is mainly through the combination of the inquiring of the patients’ genetic history, neuropsychiatric test, neuropathological diagnosis, and neuroimaging diagnosis. Only after death of AD patients, can final diagnosis be confirmed by brain tissue examination[6,7]. β-Amyloid (Aβ) hypothesis has shown that the extracellular accumulation of β-amyloid peptides forming fibrotic plaques is one of the neuropathological hallmarks of AD[8-13], as such early detection of Aβ fibrils and plaques *in vivo* with low damage plays extremely important role in the diagnosis and subsequent treatment and prevention of AD[9,14-20].

By far, a large number of imaging techniques, such as magnetic resonance imaging (MRI), positron emission tomography (PET), single photon emission computed tomography (SPECT), have been utilized to clinically diagnose AD[21]. Nevertheless, MRI can only image large plaques because of its limited sensitivity; PET needs radioisotopes which are hard to be obtained and probably impose radioactive exposure danger to patients; and SPECT has relatively higher background noise and the tracers used in this technique usually have poor blood-brain barrier (BBB) penetrating ability[1,6,15,22,23]. Drawbacks of these techniques hamper their wide application in early diagnosis of AD[11]. Compared with the above techniques, fluorescence imaging technique enjoys real-time and in-situ monitoring ability, high sensitivity, low biological toxicity, non-invasiveness, superior spatiotemporal resolution, low cost, and technical simplicity, making it promising in the imaging of Aβ fibrils and diagnosis of AD[1,7,11,23,24].

ThT, ThS, and indocyanine green (ICG) are the most commonly used fluorescent dyes to histologically stain Aβ fibrils and plaques[25]. However, the high water-solubility of these dyes limits their ability of penetrating the BBB[26,27], rendering them merely effective in *in-vitro* and *ex vivo* imaging of Aβ fibrils/plaques. Moreover, ThT is hardly able to distinguish Aβ peptides of different aggregation levels[28]. The short-wavelength excitations and emissions of probes like ThT and ThS prevent them from being used for *in-vivo* imaging, because of the unsatisfactory deep-tissue penetration ability and non-negligible phototoxicity to organisms. In addition, most of these fluorophores suffer from aggregation-caused quenching (ACQ) effect that results in self-quenching of FL signal after binding to Aβ species and the reduced detection sensitivity and imaging resolution[29]. These objective factors such as the poor specificity, less satisfactory sensitivity, small Stokes shift, relatively low reliability make these probes difficult to ensure their effectiveness in *in-vivo* imaging[7,8,30]. Sensitive and reliable probes with high ability to penetrate BBB and deep tissues which can be employed to detect Aβ fibrils and image Aβ plaques *in vivo* is urgently desirable[31].

By analyzing the structure and performance of the small-molecule fluorescent probes reported to detect Aβ fibrils and plaques, it can be found that the ones having rod-like geometric configurations and donor-acceptor (D-A) electronic structures usually perform relatively well (Fig. 1A)[1,2,14,26,32]. On the one hand, the rod-like structured probes have a certain similarity with Aβ fibrils in morphology, which is conducive to the binding of probes and Aβ fibrils and subsequently benefits the specificity. On the other hand, the probes with D-A effect are sensitive to the environmental hydrophobicity, with the emissions intensified when bound to hydrophobic areas of amyloids abundant in β-sheet structures[33-35]. Though these two essential structural features can guarantee the basic performance of the probes, other deficiencies still seriously affect the detection and imaging performance of these probes. Most of the reported probes are ACQ-active, resulting in high background and low SNR. Moreover, simple D-A structure in probes (e.g. ThT) cannot ensure red or NIR emission, which can neither avoid the interference from auto-fluorescence of organisms nor assure the penetration ability of deep tissue.

Based on the above analysis, we sort out four main criteria which should be satisfied to realize high-performance fluorescent probes for detecting and imaging Aβ fibrils and plaques *in vivo* at an early stage (Fig. 1B): (1) geometric configurations which match the β-sheet structure; (2) balanced hydrophilicity and hydrophobicity which guarantees the BBB crossing ability and high SNR; (3) strong D-A effect ensuring fluorescent response, long-wavelength excitation and emission, and large Stokes shift; (4) anti-ACQ effect that enhances the fluorescent response, SNR, and imaging resolution. In accordance with these criteria, we propose a systematic “all-in-one” strategy for rational design of high-performance *in-vivo* imaging contrast agents for precise detection of Aβ fibrils/plaques. In other words, rod-like geometric configurations, hydrophilic unit-decorated hydrophobic skeleton, large D-π-A electronic structure, and 3D flexible conformation are ingeniously integrated in one molecule to meet the above four criteria (Fig. 1B)..

As a proof of concept, AIE-CNPy-AD is designed following the “all-in-one” strategy. In this molecule, electron-donating dimethylamino, electron-accepting acetonitrile and pyridyl group are linked together via

single bonds and bridged by benzyl groups and a C=C double bond, affording a large flexible 3D rod-like configured D-π-A framework. Benefited from such a framework, strong A*β* fibril/plaque-binding capability, efficient aggregation-induced emission (AIE) effect[36] and bright red/NIR fluorescence are achieved. Furthermore, the hydrophilic propanesulfonate group is attached to the hydrophobic molecular backbone to generate the zwitterionic and amphiphilic AIE-CNPy-AD, endowing AIE-CNPy-AD with low background, high SNR and good BBB penetration ability. Since as compared with traditional ACQ probes, AIE probes often have the advantages of good photo-stability, high SNR, and resistance to photo-bleaching, the imaging performance of the fluorescent probes is greatly improved[37-40]. As a result, the rod-like amphiphilic NIR-emissive AIE probe AIE-CNPy-AD possesses excellent specificity to A*β* fibrils/plaques, superb deep-tissue penetrating ability, good resistance to auto-fluorescence interference from organisms, improved photo-stability, superior BBB penetrating capability, and high-resolution and high-contrast imaging ability.

With the aid of the above merits, the elaborated probe AIE-CNPy-AD is able to realize detection of A*β* fibrils *in vitro* with high SNR and *in-situ* mapping of A*β* plaques *in vivo* with high sensitivity, and high fidelity and contrast. More importantly, the precise *in-situ* and *in-vivo* mapping ability of A*β* plaques is not limited by mouse strains. It is worth mentioning that even small and sparsely distributed A*β* plaques in the brains of AD transgenic mice APP/PS1 as young as 4-months old could be visualized by our probe. It is reported that the A*β* plaques would not appear when the APP/PS1 mice are younger than 4-months old. Moreover, the increase and enlargement of A*β* plaques as well as the progression of AD as the mice grow could be clearly revealed by the present probe. In other words, AIE-CNPy-AD is very promising in early diagnosis and highly reliable progression monitoring of AD (Fig. 1C). To the best of our knowledge, this is the first work of harnessing the “all-in-one” strategy to rationally design AIE-active NIR imaging contrast agent for light-up and *in-situ* tracing of A*β* plaques in mice of different strains and ages. What’s more, the probe maps the A*β* plaques at the earliest stage among all the reported fluorescent probes.

Results

Rational design and facile synthesis of AIE-CNPy-AD. We make full use of the “all-in-one” strategy to pursue high-performance probes for early *in-situ* tracing of A*β* fibrils *in vivo*. As introduced above, extended D-π-A electronic architecture is built by utilizing the dimethylamino as electron-donor, the acetonitrile and pyridyl group as electron-acceptor, single bonds as linkers, and benzyl groups and C=C double bond as π-bridges, respectively. Red or even NIR emission and relatively long-wavelength excitation is supposed to result from this D-π-A structured backbone. Such a rod-like geometric configuration is envisioned to bestow the probe with strong binding affinity to A*β* fibril/plaque. Moreover, according to the principle of restriction of intramolecular motions (RIM), the multiple rotors in the skeleton would efficiently consume the excited-state energy and lead to weak or even no emission in the unconstrained state, while the distorted 3D conformation would prevent π-π stacking and self-quenching in the constrained state. It means such an AIE-active probe would give light-up response to the target species with satisfactory SNR under suitable conditions. To further reinforce the SNR, hydrophilic

propanesulfonate group is incorporated to the hydrophobic skeleton to for one thing enhance the solubility of the probe in aqueous media and thus reduce the background/noise signal, and for another to strengthen the binding between the probe and Aβ fibrils/plaques via multiple electrostatic interactions. Moreover, the considerable lipophilicity of the AIE-CNPy-AD is anticipated to be sufficient to ensure desirable BBB penetrability. The elaborately designed rod-like amphiphilic NIR-emissive zwitterionic AIE probe AIE-CNPy-AD was conveniently synthesized according to the synthetic route shown in Fig. S1 in the Electronic Supporting Information (ESI) with commercially available cheap raw materials. AIE-CNPy-AD was fully characterized with the help of ^{1}H (Fig. S2), ^{13}C NMR (Fig. S3) and high-resolution mass spectrometry (HRMS, Fig. S4).

Excellent photophysical properties facilitating the detection of Aβ fibrils/plaques. AIE-CNPy-AD showed an absorption maximum at 455 nm and an emission maximum at 720 nm (10^{-4} M) in DMSO solution (Fig. 2A), with the Stokes shift of as large as 265 nm. As AIE-CNPy-AD is soluble in highly polar solvents but aggregates in less polar solvents, DMSO was chosen as a good solvent, and THF was selected as a poor solvent to evaluate the AIE behaviors of AIE-CNPy-AD (Fig. 2 and Fig. S5). As anticipated, with the addition of THF, fluorescence enhancement was clearly observed, with the emission peak blue-shifted from 720 nm (DMSO solution) to 675 nm (DMSO/THF = 1/99, v/v), manifesting the synergistic effect of AIE and intramolecular charge transfer (ICT) (Fig. 2B). The emission intensity continuously and slowly increased when the THF fraction (f_{THF}) was no more than 60 vol%, while boosted sharply once f_{THF} reached 70 vol% (Fig. 2C). Remarkably, AIE-CNPy-AD was hardly affected by the pH value varying from 3 to 10 which covers the normal pH range of human body (Fig. S6 and Fig. 2D), suggesting the good pH stability of the fluorescence properties of our probe. Taken together, all these results undoubtedly demonstrated the remarkable AIE feature, strong ICT effect, and the stable NIR fluorescence in the aggregated state of AIE-CNPy-AD, which are conducive to the imaging of Aβ deposits.

Superb specificity and high affinity of AIE-CNPy-AD to Aβ fibrils. The binding affinity of AIE-CNPy-AD to hen egg white lysozyme (HEWL), a common model protein for amyloid studies, was evaluated first. As shown in Fig. 3A, dramatic fluorescence enhancement at 620 nm was clearly observed with the increasing concentration of fibrillar HEWL in the PBS solution. In sharp contrast, AIE-CNPy-AD displayed much less marked fluorescence response to native HEWL at the same concentration level (Fig. S7A). As compared to the emission in DMSO solution, the probe bound to HEWL showed an emission peak blue-shifted from 720 to 620 nm, which might be attributed to the ICT effect and less polar microenvironment of the protein pockets. To our satisfaction, AIE-CNPy-AD has much higher ability to distinguish fibrillar HEWL from native ones, as ThT had the same response to fibrillar and native HEWL (Fig.s 3B, 3C, and Fig. S7B). Moreover, due to the strong ACQ effect of ICG, just a small amount of fibrillar HEWL would prompt the quenching of fluorescence (Fig. S7C and Fig. 3C), making it unworkable in the detection of fibrillar HEWL. These results suggest that AIE-CNPy-AD possess higher possibility to function as a highly specific probe to Aβ fibrils in comparison to clinically used gold standard fluorescent probes such as ThT and ICG.

We then studied whether this AIE-active NIR probe could have a specific fluorescence response to Aβ fibrils. Aβ_{1-42} peptide was fully incubated to afford Aβ_{1-42} fibrils with expected fibrous or filamentous structure (Fig. 3D). When the Aβ_{1-42} fibrils were added, emission intensity of AIE-CNPy-AD increased consistently with the emission peak blue-shifted to 620 nm like the situation of binding to HEWL (Fig. 3E). Obviously, the background from AIE-CNPy-AD is far lower than that of ThT, which is merely 1/35 times that of ThT. Whereas, the signal of AIE-CNPy-AD upon interaction with Aβ_{1-42} fibrils is much higher than that of ThT under parallel conditions, which is about 1.4 times that of ThT (Fig. S8). In consequence, the SNR of AIE-CNPy-AD reached 60, which is 10 times to that of ThT (SNR_{ThT} = 6; Fig. 3F). The significantly enhanced SNR of AIE-CNPy-AD achieved by the minimization of background and amplification of signal could be interpreted as follows: (i) on one hand, the right hydrophilicity makes the AIE-CNPy-AD well dispersed in aqueous solution and the vigorous intramolecular motions efficiently exhaust the excited state, resulting in minimal emission; (ii) on the other hand, the strong binding of AIE-CNPy-AD to Aβ_{1-42} fibrils greatly hampered the intramolecular motions and activated the radiative decay channels, maximizing the fluorescence signal as a consequence of AIE effect. Ultrasensitive detection of Aβ_{1-42} fibrils could be expected.

In addition to the ultra-high SNR, AIE-CNPy-AD also has high specificity to Aβ_{1-42} fibrils. A large variety of biological species including carbohydrates, amino acids, peptides, and other proteins were employed to assess specificity of AIE-CNPy-AD to Aβ_{1-42} fibrils (Fig.3G, Fig. S9). It is evident that AIE-CNPy-AD not only hardly has response to interfering small molecular species, but also has low response to potentially competitive peptides and enzymes with large molecular weight, especially Aβ_{1-42} monomer (Fig. 3G and Fig. S9).

Apart from specificity, binding affinity of the probe to analyte is also a vital parameter that ensures accurate tracing of the Aβ_{1-42} fibrils. Displacement assay of AIE-CNPy-AD against ThT-bound Aβ_{1-42} fibrils (Fig. S10 and Fig. 3H) was then carried out to investigate the binding affinity. Fluorescence intensity of the pre-prepared ThT/Aβ_{1-42} fibrils complex was firstly recorded with excitation at 420 nm. AIE-CNPy-AD solution was subsequently added stepwise into the ThT/Aβ_{1-42} complex, and the emission intensities of these two probes were measured under excitation at their corresponding maximum absorption wavelengths. It is observed that the emission intensity of ThT at 482 nm decreased continuously with increasing concentration of AIE-CNPy-AD; and in the meantime, fluorescence of AIE-CNPy-AD peaked at 620 nm emerged and was enhanced accordingly. Remarkably, it is indicated that AIE-CNPy-AD displaced ThT from ThT/Aβ fibrils complex to generate the more strongly bound AIE-CNPy-AD/Aβ fibrils complex in the solution. Besides, dissociation constant (K_d)[41] of AIE-CNPy-AD was calculated to be 185 nM (Fig. S11), considerably smaller than that of ThT (890 nM)[42]. Sufficient evidences proved that AIE-CNPy-AD has much higher binding affinity to Aβ_{1-42} fibrils than ThT.

High-contrast and high-resolution *in-vitro* fluorescent staining of paraffin slices of mice brains. It is confirmed that AIE-CNPy-AD, with high specificity, binding affinity and SNR, exhibits excellent

performance on precise detection of Aβ_{1-42} fibrils in solution. To explore the ability of AIE-CNPy-AD to label Aβ plaques in brain tissues, *in-vitro* fluorescent staining of paraffin mice brain slices resected from 5*FAD transgenic mice, APP/PS1 transgenic mice and age-matched wild-type mice was conducted. False signals originated from the binding of AIE-CNPy-AD or antibody with proteins or interfering species in brain cells could be identified through the localization of nuclei with Hoechst 33342. Notably, as displayed in Fig. 4 and Fig. S12, no matter in 2.5-month-old 5*FAD transgenic mice or in 6-month-old APP/PS1 transgenic mice, Aβ plaques were unambiguously visualized with bright red fluorescence. Specific labeling of Aβ plaques with high contrast and high resolution in these mice indicates that AIE-CNPy-AD is universal to label Aβ plaques in different strains of mice. Moreover, it can be easily seen from the CLSM images, the Aβ plaques in 2.5-month-old 5*FAD transgenic mice (Fig. 4A and Fig. S12A-S12C) are larger and more densely distributed than that in 6-month-old APP/PS1 transgenic mice (Fig. 4F and Fig. S12D-S12F). The experimental results agreed well with situation of early plaque formation at the time point in these two strains of mice[43,44], implying the reliability of AIE-CNPy-AD in fluorescent staining of Aβ plaques in slices of mice brain. To our delight, there was no observable intracellular fluorescence signal, which implied that our probe is preferentially bound to the Aβ plaques generally forming extracellularly, eliminating the false signal from intracellular species. Simultaneously, the signals in the red channel agree fairly well with those in the green channel, manifesting that AIE-CNPy-AD has very high specificity comparable to that of antibody, to Aβ plaques (Fig. 4B-4E, 4G-4J). In contrast with transgenic mice, no plaques were found in the age-matched wild-type mice no matter observing from red or green channel (Fig. S13), which not only verified the high specificity of AIE-CNPy-AD to Aβ plaques for a second time, but also suggested the fairly high fidelity of the designed probe in real brain tissues.

***In-vivo* imaging of Aβ plaques in live mice with outstanding BBB penetrability.** Inspired by the superb red fluorescence light-up Aβ plaque-specific response in the brain slices of mice, we further evaluated the biocompatibility and BBB penetrability of AIE-CNPy-AD which is indispensable before *in-vivo* imaging. Cell viability experiments were first carried out to ascertain the biocompatibility of AIE-CNPy-AD by CCK-8 assays. Human neuroblastoma cells (SH-SY5Y), mouse brain neuroblastoma cells (Neuro-2a), mouse breast cancer cells (4T1) and human breast cancer cells (MCF-7) were incubated with different concentrations of AIE-CNPy-AD for 24 h, respectively. The cell viabilities of all these four cell lines both kept at a level close to 100% even at a probe concentration of 32 μM (Fig. S14A—Fig. S14D). The results provided strong evidence to the fact that AIE-CNPy-AD has low cytotoxicity and favorable biocompatibility to various cells, demonstrating its high applicability to live animals. The oil-water partition coefficient (log *P*) is often used as an index indicating the possible ability of penetrating BBB[45]. The log *P* of AIE-CNPy-AD was determined to be 1.24 by shaking-flask method, which is far larger than that of ThT (0.16),[8] suggestive of the higher lipophilicity and BBB penetrating potential of AIE-CNPy-AD as compared with ThT.

The feasibility of AIE-CNPy-AD tracking Aβ plaques *in vivo* was confirmed using 2.5-month-old 5*FAD mice, 6-month-old APP/PS1 mice and age-matched wild-type mice as model mice. Live imaging of these mice was performed after the tail vein injection of AIE-CNPy-AD (Fig. 5). Almost all the fluorescence

signals were clearly witnessed in the center of brain compartments and able to be efficiently captured. Apparently, the fluorescence signals in the brain regions of 2.5-month-old 5*FAD mice (Fig. 5A) were already much stronger than those in the wild-type mice at 5 min post injection (Fig. 5B). Particularly, with the decay of signal, difference in signal intensity recorded from 5*FAD and wild-type mice was enlarged as indicated by the semi-quantitative analysis of the images (Fig. 5E). Similarly, intense fluorescence signal is readily visible from the brain area of 6-month-old APP/PS1 mice after the injection of AIE-CNPy-AD. Moreover, the contrast between the fluorescence signals from APP/PS1 and 6-month-old wild-type mice is quite dramatic. Compared with 5*FAD mice, difference in the signal intensity between APP/PS1 mice and age-matched wild-type mice was 4.7 times larger than that between 5*FAD mice and the corresponding wild-type mice at 5 min after being injected with AIE-CNPy-AD (Fig. 5G, 5H, and 5K). It might be because the formation of Aβ deposits in APP/PS1 mice is slower than that in 5*FAD mice. In addition, fluorescence signal intensity of APP/PS1 mice declined faster than that of 5*FAD mice after being injected with AIE-CNPy-AD for 30 min, as it can be seen from the semi-quantitative analysis of the images (Fig. 5K). It is possibly because that there are larger and more Aβ plaques in 2.5-month-old 5*FAD mice than in 6-month-old APP/PS1 mice, which slows down the clearance of AIE-CNPy-AD from the brain. Notably, whether in 5*FAD mice or APP/PS1 mice at 1 h post probe injection, F(t)/F(Pre) value of transgenic mice was at least 1.75 times that of wild-type mice, indicative of the potential of AIE-CNPy-AD to realize long-term tracking of Aβ plaques *in vivo*.

The case as for ThS is very different from that of AIE-CNPy-AD. As shown in Fig. 5C, 5D, 5F, 5I, 5J, and 5L, hardly any valid signal was found from the 5*FAD mice, APP/PS1 mice and wild-type mice administrated with ThS, clearly revealing the powerlessness of ThS in *in-vivo* imaging of Aβ plaques. This most probably results from the combination of its poor BBB permeability, short excitation and emission wavelengths which cannot penetrate the skull of mice, and the ACQ effect[46]. Undoubtedly, these visualization results directly validated that AIE-CNPy-AD is capable of penetrating the BBB and imaging Aβ fibrils/plaques *in vivo* with high contrast and fidelity.

***In-vivo* tracking of Aβ plaques in APP/PS1 mice at a very early stage**. It has confirmed that AIE-CNPy-AD exhibits significant signal difference between transgenic mice and wild-type mice in a relatively long time-period post probe administration. It can be envisaged that AIE-CNPy-AD might be promising for early diagnosis of AD in transgenic mice by virtue of the Aβ plaques-sepecific *in-vivo* imaging ability of AIE-CNPy-AD. Young APP/PS1 transgenic mice of 2-month-, 3-month-, 4-month-, and 6-month-old and age-matched wild-type (WT) mice were thus employed to systematically assess the performance of AIE-CNPy-AD in early diagnosis of AD (Fig. 6 and Fig. S15). It was observed that the difference in the fluorescence signal intensity of APP/PS1 transgenic mice and wild-type mice already became very evident at the age of 4 month. In the meantime, the fluorescence signal intensity is positively correlated with the age of transgenic AD mice (Fig. 6A). More specifically, at 20 min post injection, the F(t)/F(Pre) value of the 4-month-old APP/PS1 transgenic mice was 1.86 times that of the age-matched WT mice, and the F(t)/F(Pre) value of 6-month-old APP/PS1 transgenic mice was 2.06 times that of the age-matched WT mice (Fig. 6B). Meanwhile, there was no apparent signal difference in WT mice of different months (Fig.

6C), and the *F*(t)/*F*(Pre) values of 2-month-old and 3-month-old APP/PS1 transgenic mice were almost the same as those of the age-matched WT mice (Fig. 6D). These imaging results especially those acquired with APP/PS1 transgenic mice at an age of 4-month-old clearly showed that AIE-CNPy-AD is competent for the precise diagnosis of AD at a super-early stage. It has been speculated that the reason for the failure of early drug intervention on AD is probably that intervention in the phase is not early enough, which in turn is greatly related to the efficient capture of biological manifestations rather than clinical manifestations in the early diagnosis[47,48]. The experimental results obtained with AIE-CNPy-AD is of great significance because APP/PS1 transgenic mice are found to exhibit memory deficits from 5 months old on which is early clinical presentations, confirming that AIE-CNPy-AD can diagnose AD of APP/PS1 transgenic mice during the period of early biological manifestations, prior to the appearance of clinical presentations[43,47,49]. Furthermore, as shown in Fig. S16, ThS could neither give discriminatory signals between the APP/PS1 transgenic mice and wild-type mice nor provide distinct signals among mice of different ages, manifesting that our probe outperforms the clinically used gold-standard probe and could be used as an upgraded alternative to the commercially available ones.

It is worth mentioning that AIE-CNPy-AD does not only hold satisfactory cytocompatibility with negligible toxicity to diverse cells including neuronal cell lines but also has outstanding *in-vivo* biocompatibility as suggested by Fig. S17. The H&E staining results of the heart, liver, spleen, lung, kidney, and brain slices resected from 5*FAD (2-month-old), APP/PS1 (6-month-old) transgenic mice, and wild-type mice (6-month-old) at 24 h post the administration with AIE-CNPy-AD via tail vein injection are almost identical to those injected with PBS buffer under parallel conditions. It manifests that AIE-CNPy-AD does not cause obvious necrosis to tissues, suggesting the superb *in-vivo* biocompatibility of the present probe. The Tunel results of the brain slices further verifies this as there is no evident apoptosis being observed in all the samples. Therefore, in view of the very low toxicity to cells and tissues, the AIE-CNPy-AD is proven to be highly suitable for *in-vivo* detection and has great potential in clinical use.

***Ex-vivo* observation of frozen brain slices of mice pre-administrated with AIE-CNPy-AD further validates its high fidelity of Aβ plaques-specific imaging.** To further examine whether the AIE-CNPy-AD binds exclusively to Aβ plaques in the brain of live mice, the APP/PS1 transgenic mice of different ages and age-matched wild-type mice were injected with AIE-CNPy-AD and sacrificed at 15 min post-administration. The frozen slices of these mice brain were then stained with rabbit anti-mouse primary antibody (ab201060), Alexa Fluor® 488-labeled goat anti-rabbit secondary antibody (ab150077), and Hoechst 33342 in sequence. As shown in Fig. 7A, 7F, and Fig. S17, the Aβ plaques were imaged with high resolution and high contrast. Moreover, it can be clearly observed that the Aβ plaques in brain slices of 6-month-old APP/PS1 transgenic mice were larger and richer in number than those of 4-month-old APP/PS1 transgenic mic, while no significant Aβ plaques were found in the brain slices of 2-month-old, 3-month-old APP/PS1 transgenic mice (Fig. S18), and all the age-matched WT mice (Fig. S19). Manifestly, AIE-CNPy-AD indeed labelled Aβ plaques *in vivo* with ultrahigh fidelity and specificity, as suggested by the very good overlap between the green (antibody) and red channels (AIE-CNPy-AD; Fig. 7B-7E and 7G-7J).

Elucidation of the working mechanism with molecular docking simulations. We believe that the rod-like architecture, extended D-π-A electronic structure, flexible 3D conformation, the amphiphilic and zwitterionic molecular structure collectively contribute to the outstanding performance of AIE-CNPy-AD in Aβ fibrils/plaques-specific detection and imaging. As above mentioned, the rod-like structure is supposed to favors the recognition of β sheets. Moreover, the hydrophobic π-conjugated backbone and the pyridyl and sulfonate groups are envisaged to benefit the binding of AIE-CNPy-AD to Aβ species possibly via hydrophobic interaction, π-π interaction, and electrostatic interaction. When in solution or molecularly dispersed, the AIE-CNPy-AD molecules undergo active intramolecular motions, leading to an OFF state and a low background. When coexists with Aβ monomer, intramolecular motions of AIE-CNPy-AD are merely weakly restricted, rendering weak red emission released (near-OFF state), due to the weak binding affinity of AIE-CNPy-AD and Aβ monomer. On the contrary, strong interactions between AIE-CNPy-AD and fibrils impose severe restriction on the intramolecular motions, which activates the AIE process[50,51], and switches AIE-CNPy-AD from OFF to ON state to emit strong red/NIR fluorescence. Thus, AIE-CNPy-AD can distinguish Aβ fibrils from Aβ monomers precisely (Fig. 8A).

Molecular docking simulations were carried out to unveil the interactions between AIE-CNPy-AD and Aβ fibrils or monomer and to elucidate the working mechanism of specific detection of Aβ fibrils. As revealed by the three top docking conformations with the lowest binding free energies shown in Fig. 8B, 8C and Fig. S20, the most preferable binding direction of AIE-CNPy-AD to Aβ fibrils is consistent with the orientation of the β-sheets of Aβ fibrils, which proves that rod-shaped geometric structure of AIE-CNPy-AD is very helpful to the binding with Aβ fibrils[53]. Simultaneously, the hydrophobic PHE-19 residue on the β-sheets of Aβ fibrils has strong C-H···π interaction (2.6 Å) with the phenyl ring of AIE-CNPy-AD, and the ALA-21 residue exhibits very strong interaction with the cyano group of AIE-CNPy-AD (2.2 Å). To our astonishment, the GLY-25 residue and two LYS-28 residues have strong hydrogen bonding interactions with the sulfonate group of AIE-CNPy-AD (1.7–2.1 Å). It is obvious that sulfonate not only improves water solubility of AIE-CNPy-AD, but also further enhances the binding ability of AIE-CNPy-AD to Aβ fibrils via H-bonding and electrostatic interactions. Collectively, the strong intermolecular interactions between AIE-CNPy-AD and Aβ fibrils greatly hinder the intramolecular motions of AIE-CNPy-AD to give out the “lighted-up” fluorescent response[54].

In contrast, only the LYS-28 residue of Aβ monomer shows hydrogen bonding interaction with the sulfonate unit of AIE-CNPy-AD and no other interactions exist, which results in weaker restriction on the intramolecular motions and weak fluorescence (Fig. 8D and Fig. 8E). The inhibition constant (K_i)[55] of AIE-CNPy-AD and Aβ fibrils (935 nM) is far smaller than that of AIE-CNPy-AD and Aβ monomer (45.0 μM). Simultaneously, the lowest docking energy of AIE-CNPy-AD and Aβ fibrils was calculated to be -8.23 kcal/mol, which is substantially lower than that of AIE-CNPy-AD and Aβ monomer (-5.93 kcal/mol). As exhibited in Table S1, all the ten best binding poses with the lowest energies of AIE-CNPy-AD and Aβ fibrils consistently display lower docking energies than those of AIE-CNPy-AD and Aβ fibrils. These data sufficiently suggested that binding affinity of AIE-CNPy-AD to Aβ fibrils is much stronger than that of AIE-CNPy-AD to Aβ monomer. Moreover, the binding energy of AIE-CNPy-AD and Aβ fibrils is lower than that of

ThT and Aβ fibrils (-7.18 kcal/mol)[56], indicating that the AIE-CNPy-AD possesses higher affinity to Aβ fibrils as compared to ThT. The molecular docking simulation results are powerful proofs to our experiment results and further verify the rationality and feasibility of our design strategy.

Discussion

Precise *in-vivo* tracking of Aβ fibrils/plaques is of great significance in both fundamental research and technological development. In this work, we proposed an 'all-in-one' molecular design strategy and implemented it in the development of a novel AIE-active NIR-emissive probe (AIE-CNPy-AD) for specifically discriminating Aβ fibrils and imaging Aβ plaques *in vivo* at an early stage. Rod-shaped amphipathic AIE-CNPy-AD possesses excellent BBB penetrability and high binding affinity to Aβ fibrils. The D-π-A electronic structure with multiple rotors and flexible 3D conformations endues AIE-CNPy-AD with red/NIR emission, AIE feature, and resultant excellent *in-vivo* tracing capability of Aβ fibrils with superior tissue penetration ability, high signal-to-noise ratio and high fidelity. More importantly, our probe also enjoys the following advantages: (1) it is simple in structure, facile in preparation with cheap raw materials, and low in cost; (2) the *in-vivo* imaging capability is universal and not restricted by the strain of mouse; (3) the precise *in-vivo* tracking of Aβ fibrils could be realized at a very early stage before the occurrence of clinical manifestations; (4) the probe maps the Aβ plaques at the earliest stage as compared to all the reported fluorescent probes; (5) the cytocompatibility and *in-vivo* compatibility is satisfactory for *in-vivo* investigation and clinical application (Table S2). Moreover, the rationality and feasibility were fully verified and the working mechanism of AIE-CNPy-AD was elucidated by the molecular docking simulation results. The present work will not only shed light on the rational design of high-performance fluorescent probes for accurately imaging of Aβ fibrils *in vivo*, but also provide a promising diagnostic tool to diagnose AD at an early stage and find timing of early drug intervention.

Methods

Materials and instruments. Conventional reagents and raw materials, purchased from formal channels, are analytically pure and used without further purification. Aβ_{1-42} peptides were purchased from GL Biochem (Shanghai) Co., Ltd. Hen egg white lysozyme (HEWL) was purchased from Aladdin. Cell culture medium RPMI-1640, penicillin-streptomycin, and 0.25% trypsin were obtained from M&C Gene Technology (Beijing, China). Fetal bovine serum was purchased from Gemini Bio-Products (Calabasas, California, USA). All other solvents and reagents for biological experiments were of analytical grade.

The molecular structures were characterized using ^{1}H NMR, ^{13}C NMR and high-resolution mass spectroscopy. ^{1}H NMR and ^{13}C NMR spectra were recorded on a Brüker AV-400 spectrometer by using deuterated solvents with 0.03% TMS as internal standard. The high-resolution mass spectra were taken on an HP 5958 mass spectrometer with the electronic spray ionization mode. The UV-Vis absorption spectra were recorded in 1 cm slit quartz cells on an Agilent Cary 60 UV-Vis spectrometer. The photoluminescence spectra were recorded in 1 cm or 4 mm-slit quartz cells on an Agilent Cary Eclipse

Fluorescence spectrophotometer. Photographs were taken with a Canon EOS 6D digital camera. Buffer solutions were prepared with Mettler Toledo FE28-Bio. Aβ fibrils samples were prepared by sonication in a SB-800DT water-bath sonicator and vortexed by digital Vortex-Genie® 2 mixer. TEM images were obtained on a JEM-1400 biological transmission electron microscope. Fluorescent images of brain slices were obtained by a confocal laser scanning microscope (CLSM, Nikon, Japan). The live mice were imaged with a LivingImage system and the relative fluorescence intensity was analyzed by LivingImage 4.3.1 software (Caliper).

Synthesis of AIE-CNPy-AD. (*Z*)-3-(4-(Dimethylamino)phenyl)-2-(4-(pyridin-4-yl)phenyl)acrylonitrile (PyDPACN-N) is synthesized according to the literature.[57] **1** (294 mg, 1.5 mmol), **2** (268 mg, 1.8 mmol), sodium hydroxide (72 mg, 1.8 mmol) and EtOH (20 mL) were added into a 100 mL two-necked round-bottomed flask. The flask was flushed with dry nitrogen for three times. Then the mixture was stirred overnight at room temperature. Yellow solids were filtered out and washed thoroughly with EtOH to yield **3** (Fig. S1).

3 (98 mg, 0.30 mmol), **4** (44 mg, 0.36 mmol), $Pd(PPh_3)_4$ (17 mg, 0.015 mmol), 2 M K_2CO_3 solution (2 mL) and THF (10 mL) were added into a 100 mL two-necked round-bottomed flask. The flask was flushed with dry nitrogen for three times. Then the mixture was heated to 85 ^oC for 12 h. After the termination of the reaction, the resultant mixture was extracted with DCM for three times, and the collected organic layers was concentrated by a rotatory evaporator. Then the crude product was purified by column chromatography to obtain PyDPACN-N (Fig. S1).

PyDPACN-N (164 mg, 0.5 mmol), sodium 3-bromopropanesulfonate (**5**, 225 mg, 2.0 mmol), and CH_3CN (20 mL) were added into a 100 mL two-necked round-bottomed flask. The flask was flushed with dry nitrogen three times. Then the mixture was refluxed for 96 h. Solids were filtered out from cooled mixture, and washed thoroughly with THF and water to afford the target product.

Preparation of fibrillar HEWL. Lyophilized HEWL was dissolved at 14 mg/mL (1 mM) in sodium acetate–acetic acid buffer with 0.1 M NaCl (10 mM, pH = 3)[58]. The solution was incubated in an oil bath at 70 ^oC and magnetically stirred at 250 rpm for 12 h. The initially clear solution was observed to form cloudy aggregates by 1 h of incubation. The samples were stored at 4 ^oC.

Preparation of Aβ_{1-42} fibrils. Aβ_{1-42} (0.25 mg) was dissolved in hexafluoroisopropanol (HFIP) and sonicated in a water-bath sonicator for 5 min at room temperature[59]. HFIP-treated solution was vortexed gently and incubated for 45 min at room temperature. After chilling solution on ice, the solvent was removed in a dry nitrogen stream. Dimethyl sulfoxide and PBS buffer (pH = 7.4) was added to the pretreated peptide film to afford a 0.2 mM solution, which was further incubated at 37 ^oC and shaken for 7 days to yield the desired samples of Aβ_{1-42} fibrils.

Transmission electron microscopy (TEM) test of Aβ_{1-42} fibrils. 1 μL aged Aβ_{1-42} fibrils solution (0.2 mM) was added into water to dilute to 10 μM solution. Samples for TEM measurement were prepared by

depositing 10 μL of the appropriate solution onto a carbon-coated copper grid, keeping at room temperature for 20 min to ensure the adsorption of Aβ_{1-42} fibrils on the copper grid, and wicking the excess solution away with a small piece of filter paper. The samples were then stained with phosphotungstic acid. At last, the sample grids were allowed to be dried at room temperature and imaged on a JEM-1400 biological transmission electron microscope.

Cell lines for cytotoxicity assay. The human neuroblastoma cells (SH-SY5Y), mouse brain neuroblastoma cells (Neuro-2a), mouse breast cancer cells (4T1) and human breast cancer cells (MCF-7) were obtained from the Institute of Basic Medical Science (Beijing, China). SH-SY5Y cells were cultured in DMEM/F-12 medium. Neuro-2a cells were cultured in DMEM with high glucose medium. 4T1 and MCF-7 cells were cultured in RPMI-1640 medium. All of the above media were supplemented with 10% fetal bovine serum and 1 % (100 U/mL) penicillin-streptomycin at 37 ^{o}C in 5% CO_2 atmosphere.

***In-vitro* cytotoxicity assay.** The cytotoxicity of AIE-CNPy-AD was investigated by Cell Counting Kit-8 (CCK-8) assay (Dojindo, Tokyo, Japan) according to the instruction manual. Briefly, human neuroblastoma cells (SH-SY5Y cells) were seeded into a 96-well plate at a density of 5000 cells/well for 24 h. Serial concentrations of AIE-CNPy-AD (0-32 μM, 200 μL/well) were added to treat cells. After being incubated for 24, culture medium with AIE-CNPy-AD was withdrawn, and then a fresh medium containing 10 μL of CCK-8 reagent was added to each well. Cells were incubated for another 3 h at 37 ^{o}C in 5% CO_2 atmosphere. The absorbance at 450 nm was measured by a micro-plate reader (SpectraMAX 190, Molecular Devices). The cell viability was calculated using GraphPad Prism 7.0 software. The cytotoxicity assay procedures of mouse brain neuroblastoma cells (Neuro-2a), mouse breast cancer cells (4T1), and human breast cancer cells (MCF-7) are the same as that of SH-SY5Y, except that the number of the other three cells inoculated in 96-well plates was 10,000.

Animals. 5*FAD transgenic mice (C57BL/6J, 2, 2.5-month-old), APP/PS1 transgenic mice (C57BL/6J, 2, 3, 4, and 6-month-old) and age-matched wild-type mice (C57BL/6J, 2, 2.5, 3, 4, and 6-month-old) were purchased from Beijing Hua fu kang Biotechnology Co., Ltd. (Beijing, China). Care and hand-lings of all mice were adhered to the approval of Institutional Animal Care and Use Committee of East China University of Science & Technology (Assigned approval no: ECUST-2020-04014).

***In-vitro* fluorescence staining of mice brain slices using AIE-CNPy-AD**. *In-vitro* fluorescence staining of mice brain slices was performed to verify the binding ability of AIE-CNPy-AD to Aβ_{1-42} aggregates. 5*FAD transgenic mice, APP/PS1 transgenic mice and age-matched wild-type mice were sacrificed with cold saline perfusion for 15 min without administration of AIE-CNPy-AD. Brain tissues were dissected, fixed in 4% paraformaldehyde overnight, and dehydrated in 30% sucrose. Then the tissues were embedded with paraffin cut into 8 μm serial sections, and stored at −80 ^{o}C before use. Pre-prepared paraffin-embedded 4 μm brain tissue sections from 5*FAD transgenic mice (C57BL/6J, 2.5-month-old), APP/PS1 transgenic mice (C57BL/6J, 2, 3, 4, and 6-month-old) and age-matched wild-type mice (C57BL/6J, 2, 2.5, 3, 4, and 6-month-old) were used for *in-vitro* fluorescence staining. The tissue slices were baked in an incubator at 60 ^{o}C for 60 min to prevent stripping. After being cooled to room temperature, the slices were deparaffinized

by immersion in xylene, followed by washing with different gradients of ethanol and water. Then the sections were heated to 95 ^{o}C in ethylene diamine tetraacetic acid (EDTA) antigen retrieval buffer for 20 min. After cooling, the sections were incubated in the aqueous solution of AIE-CNPy-AD (100 μM) at 37 ^{o}C for 20 min, and then washed with PBS buffer. The sections were blocked with 3% BSA solution at 37 ^{o}C for 60 min, permeabilized with 0.1% (v/v) Triton X-100 for 3 min at room temperature, then incubated with rabbit anti-mouse primary antibody (ab201060, diluted by 1:200 with PBS buffer) at 4 ^{o}C overnight. Sections that were incubated only with 3% BSA were served as controls. After being washed 3 times with PBS buffer, all sections were stained with Alexa Fluor® 488-labeled goat anti-rabbit secondary antibody (ab150077, 1:1000) at 37 ^{o}C for 60 min. After being washed 3 times with PBS buffer, anti-fluorescence quenching mounting solution containing Hoechst 33342 was added. Finally, samples were observed under a confocal laser scanning microscope (CLSM, Heidelberg, Germany), using the following conditions: Hoechst 33342: λ_{ex} = 405 nm, λ_{em} = 461 nm; Alexa Fluor® 488: λ_{ex} = 495 nm, λ_{em} = 519 nm; AIE-CNPy-AD: λ_{ex} = 500 nm, λ_{em} = 620 nm)

Real-time *in-vivo* imaging in transgenic mice. The live imaging experiments were conducted to observe the distribution of AIE-CNPy-AD in brains. Before *in-vivo* imaging, the heads of transgenic mice of different ages and age-matched wild-type mice were shaved and cleaned. The background fluorescence was captured by LivingImage system before the administration of AIE-CNPy-AD. Then AIE-CNPy-AD was injected to transgenic mice and age-matched wild-type mice (3 mice per group) via tail vein (2.0 mg kg^{-1}, 5.5% DMSO, 94.5% PBS buffer, 400 μL). In addition, the control groups of mice were injected with commercially available ThS. Then mice were anaesthetized by isoflurane and photographed by LivingImage system at pre-set time points (AIE-CNPy-AD, λ_{ex} = 500 nm, λ_{em} = 620 nm; ThS, λ_{ex} = 430 nm, λ_{em} = 500 nm). The relative fluorescence intensity was analyzed by LivingImage 4.3.1 software (Caliper).

Evaluation of the *in-vivo* biocompatibility of AIE-CNPy-AD. 5*FAD (2-month-old), APP/PS1 (6-month-old) transgenic mice, and wild-type mice (6-month-old) were chosen as models and were injected with AIE-CNPy-AD or PBS buffer via tail vein injection, then sacrificed with cold saline perfusion at 24 h after administration. Heart, liver, spleen, lung, kidney, and brain tissues were dissected from the above mice, fixed in 4% paraformaldehyde overnight, and dehydrated in 30% sucrose. Then the tissues were embedded with paraffin cut into 8 μm serial sections, and stored at −80 ^{o}C before use. All the tissue slices were observed using hematoxylin-eosin staining. The brain slices were also observed utilizing TdT-mediated DUTP Nick-End Labeling (Tunel) technique to detect the apoptosis.

***Ex-vivo* observation for fluorescence signals of the brain slices of mice intravenously injected with AIE-CNPy-AD.** APP/PS1 transgenic mice of different ages and age-matched wild-type mice were injected with AIE-CNPy-AD, then sacrificed with cold saline perfusion at 15 min after administration. Brain tissues were dissected, fixed in 4% paraformaldehyde overnight, and dehydrated in 30% sucrose. Then the tissues were embedded with OCT (optimum cutting temperature embedding medium), cut into 8 μm serial sections, and stored at −80 ^{o}C before use. The sections were blocked with 3% BSA solution at 37°C for 60 min, permeabilized with 0.1% (v/v) Triton X-100 for 3 min at room temperature, then incubated with rabbit anti-

mouse primary antibody overnight at 4°C. After being washed 3 times with PBS buffer, all sections were stained with Alexa Fluor® 488-labeled goat anti-rabbit secondary antibody at 37 °C for 60 min, followed by the addition of anti-fluorescence quenching mounting solution containing Hoechst 33342. Finally, samples were observed with a confocal laser scanning microscope (CLSM, Heidelberg, Germany). (Hoechst 33342, λ_{ex} = 405 nm, λ_{em}: 461 nm; Alexa Fluor® 488, λ_{ex} = 495 nm, λ_{em} = 519 nm; AIE-CNPy-AD: λ_{ex} = 500 nm, λ_{em} = 620 nm).

Docking simulations and analysis. The structure of AIE-CNPy-AD was optimized with a B3LYP/6-31+G* basis set using the Gaussian 09 package[60]. The structures of the Aβ_{1-42} fibrils (PDB ID: 2BEG[61]) and the Aβ_{1-42} monomer (PDB ID: 1Z0Q[62]) were obtained from the Protein Data Bank[63]. AutoDockTools 1.5.7 [64] was employed to molecular docking simulation and the dimensions of the grids were 126 Å × 68 Å × 74 Å for Aβ fibrils (spacing: 0.375 Angstrom) and 126 Å × 64 Å × 60 Å for Aβ monomers (spacing: 0.464 Angstrom). We used the Lamarckian genetic algorithm and a standard protocol to conduct calculations on the binding energies and modes of AIE-CNPy-AD to Aβ fibrils or Aβ monomer. The calculation results were analyzed by PyMOL (version 2.3.1)[65].

Declarations

Notes

The authors declare no competing interests.

Acknowledgements

We are grateful for the financial support from the NSFC/China (Nos. 21788102, 21875064, 81903545, 21604023, and 21790361), Shanghai Municipal Science and Technology Major Project (No. 2018SHZDZX03), Programme of Introducing Talents of Discipline to Universities (No. B16017), Shanghai Science and Technology Committee (No. 17520750100), Beijing New-Star Plan of Science and Technology (No. Z201100006820009), the Shanghai Sailing Program (No. 16YF1402200), and the Fundamental Research Funds for the Central Universities.

Author contributions

Y.W. and D.M. contributed equally to this work. J.M. concepted and designed this work, Y.W. conducted the synthesis, characterization and the *in-vitro* evaluation of the probe. D.M. performed the *in-vivo* imaging experiments and the biocompatibility evaluation. X.Z. performed the DFT calculation and molecular docking simulation. J.M., D.M., Y.W., H.T., and D.H.Q. analyzed and interpreted the data. J.M., Y.W., D.M., H.T. wrote and revised the article. All authors participated in drafting the manuscript and approved the final version of the manuscript.

References

1. Yang, J. et al. Development of near-infrared fluorescent probes for use in Alzheimer's disease diagnosis. *Bioconjug. Chem.* **31**, 2–15 (2020).
2. Aliyan, A. et al. Interrogating amyloid aggregates using fluorescent probes. *Chem. Rev.* **119**, 11819–11856 (2019).
3. Zhou, K. et al. Smart D-π-A type near-infrared A*β* probes: Effects of a marked π bridge on optical and biological properties. *Anal. Chem.* **89**, 9432–9437 (2017).
4. Li, Y. et al. A theranostic agent for in vivo near-infrared imaging of *β*-amyloid species and inhibition of *β*-amyloid aggregation. *Biomaterials* **94**, 84–92 (2016).
5. Cai, J. et al. Ultrasmall T1-T2 magnetic resonance multimodal imaging nanoprobes for the detection of *β*-amyloid aggregates in Alzheimer's disease mice. *ACS Appl. Mater. Interfaces* **12**, 26812–26821 (2020).
6. Fernandez, T. et al. Functionalization and characterization of magnetic nanoparticles for the detection of ferritin accumulation in Alzheimer's disease. *ACS Chem. Neurosci.* **9**, 912–924 (2018).
7. Cui, M. et al. Smart near-infrared fluorescence probes with donor-acceptor structure for *in vivo* detection of *β*-amyloid deposits. *J. Am. Chem. Soc.* **136**, 3388–3394 (2014**)**.
8. Fu, W. et al. Rational design of near-infrared aggregation-induced-emission-active probes: In situ mapping of amyloid-*β* plaques with ultrasensitivity and high-fidelity. *J. Am. Chem. Soc.* **141**, 3171–3177 (2019).
9. Wang, J. et al. Enhanced photoresponsive graphene oxide-modified *g*-C_3N_4 for disassembly of amyloid *β* fibrils. *ACS Appl. Mater. Interfaces* **11**, 96–103 (2019).
10. Xia, N. et al. Visual and fluorescent assays for selective detection of *β*-amyloid oligomers based on the inner filter effect of gold nanoparticles on the fluorescence of CdTe quantum dots. *Biosens. Bioelectron.* **85**, 625–632 (2016).
11. Fu, H. et al. Amyloid-*β* deposits target efficient near-infrared fluorescent probes: Synthesis, *in vitro* evaluation, and *in vivo* imaging. *Anal. Chem.* **88**, 1944–1950 (2016).
12. Li, Y. et al. Fluoro-substituted cyanine for reliable *in vivo* labelling of amyloid-*β* oligomers and neuroprotection against amyloid-*β* induced toxicity. *Chem. Sci.* **8**, 8279–8284 (2017).
13. Heo, C. H. et al. A quadrupolar two-photon fluorescent probe for *in vivo* imaging of amyloid-*β* plaques. *Chem. Sci.* **7**, 4600–4606 (2016).
14. Peng, C. et al. Versatile fluorescent probes for near-infrared imaging of amyloid-*β* species in Alzheimer's disease mouse model. *J. Mater. Chem. B* **7**, 1986–1995 (2019).
15. Wang, Y. L. et al. AIE-based super-resolution imaging probes for *β*-amyloid plaques in mouse brains. *Mater. Chem. Front.* **2**, 1554–1562 (2018).
16. Dou, W. T. et al. Fluorescence imaging of Alzheimer's disease with a flat ensemble formed between a quinoline-malononitrile AIEgen and thin-layer molybdenum disulfide. *ChemBioChem* **20**, 1856–1860 (2019).

17. Zhao, Y. et al. A simple aptasensor for Aβ_{40} oligomers based on tunable mismatched base pairs of dsDNA and graphene oxide. *Biosens. Bioelectron.* **149**, 111840 (2020).
18. Zhou, K. et al. Structure-property relationships of polyethylene glycol modified fluorophore as near-infrared Aβ imaging probes. *Anal. Chem.* **90**, 8576–8582 (2018).
19. Saini, M. et al. Two instantaneous fluorogenic steps for detection of nanomolar amyloid β monomer and its interaction with stoichiometric copper(II) ion. *Sens. Actuat. B Chem.* **303**, 127086 (2020).
20. Fanni, A. M. et al. High selectivity and sensitivity of oligomeric *p*-phenylene ethynylenes for detecting fibrillar and prefibrillar amyloid protein aggregates. *ACS Chem. Neurosci.* **10**, 1813–1825 (2019).
21. Tan, H. Y. et al. Dual-functional red-emitting fluorescent probes for imaging β-amyloid plaques and viscosity. *Sens. Actuators B Chem.* **298**, 126903 (2019).
22. Yan, J. W. et al. Neutral merocyanine dyes: For *in vivo* NIR fluorescence imaging of amyloid-β plaques. *Chem. Commun.* **53**, 9910–9913 (2017).
23. Watanabe, H. et al. *In vivo* fluorescence imaging of β-amyloid plaques with push-pull dimethylaminothiophene derivatives. *Chem. Commun.* **51**, 17124–17127 (2015).
24. Fu, H. et al. *In vivo* near-infrared and Cerenkov luminescence imaging of amyloid-β deposits in the brain: A fluorinated small molecule used for dual-modality imaging. *Chem. Commun.* **52**, 12745–12748 (2016).
25. Leung, C. W. et al. Detection of oligomers and fibrils of α-synuclein by AIEgen with strong fluorescence. *Chem. Commun.* **51**, 1866–1869 (2015).
26. Cheng, Y. et al. *In vivo* detection of cerebral amyloid fibrils with smart dicynomethylene-4*H*-pyran-based fluorescence probe. *Anal. Chem.* **87**, 4781–4787 (2015).
27. Staderini, M. et al. Imaging of β-amyloid plaques by near infrared fluorescent tracers: A new frontier for chemical neuroscience. *Chem. Soc. Rev.* **44**, 1807–1819 (2015).
28. Hatai, J. et al. Analyzing amyloid β aggregates with a combinatorial fluorescent molecular sensor. *J. Am. Chem. Soc.* **139**, 2136–2139 (2017).
29. Yang, Y. et al. An AIE-active theranostic probe for light-up detection of Aβ aggregates and protection of neuronal cells. *J. Mater. Chem. B* **7**, 2434–2441 (2019).
30. Shin, J. et al. Harnessing intramolecular rotation to enhance two-photon imaging of Aβ plaques through minimizing background fluorescence. *Angew. Chem. Int. Ed.* **58**, 5648–5652 (2019).
31. Hong, Y. et al. Monitoring and inhibition of insulin fibrillation by a small organic fluorogen with aggregation-induced emission characteristics. *J. Am. Chem. Soc.* **134**, 1680–1689 (2012).
32. Jun, Y. W. et al. Frontiers in probing Alzheimer's disease biomarkers with fluorescent small molecules. *ACS Cent. Sci.* **5**, 209-217 (2019).
33. Benzeid, H. et al. A thienoquinoxaline and a styryl-quinoxaline as new fluorescent probes for amyloid-β fibrils. *C. R. Chim.* **15**, 79-84 (2012).
34. Ono, M. et al. BODIPY-based molecular probe for imaging of cerebral β-amyloid plaques. *ACS Chem. Neurosci.* **3**, 319-324 (2012).

35. Klunka, W. E. et al. Uncharged thioflavin-T derivatives bind to amyloid-β protein with high affinity and readily enter the brain. *Life Sci.* **69**, 1471-1484 (2001).
36. Luo, J. et al. Aggregation-induced emission of 1-methyl-1,2,3,4,5-pentaphenylsilole. *Chem. Commun.* 1740–1741 (2001).
37. Mei, J. et al. Aggregation-induced emission: The whole is more brilliant than the parts. *Adv. Mater.* **26**, 5429–5479 (2014).
38. Pradhan, N. et al. Detection and monitoring of amyloid fibrillation using a fluorescence "switch-on" probe. *ACS Appl. Mater. Interfaces* **7**, 25813–25820 (2015).
39. Mei, J. et al. Progress and trends in AIE-based bioprobes: A brief overview. *ACS Appl. Mater. Interfaces* **10**, 12217–12261 (2018).
40. Mei, J. et al. Aggregation-induced emission: Together we shine, united we soar! *Chem. Rev.* **115**, 11718–11940 (2015).
41. Rajasekhar, K. et al. A high affinity red fluorescence and colorimetric probe for amyloid β aggregates. *Sci. Rep.* **6**, 23668 (2016).
42. Diner, I. et al. Generation of clickable pittsburgh compound B for the detection and capture of β-amyloid in Alzheimer's disease brain. *Bioconj. Chem.* **28**, 2627 (2017).
43. Zhu, S. et al. The role of neuroinflammation and amyloid in cognitive impairment in an APP/PS1 transgenic mouse model of Alzheimer's disease. *CNS Neurosci. Ther.* **23**, 310–320 (2017).
44. Oakley, H. et al. Intraneuronal β-amyloid aggregates, neurodegeneration, and neuron loss in transgenic mice with five familial Alzheimer's disease mutations: Potential factors in amyloid plaque formation. *J. Neurosci.* **26**, 10129–10140 (2006).
45. Ametamey, S. M. et al. Molecular imaging with PET. *Chem. Rev.* **108**, 1501–1516 (2008).
46. Law, A. S. et al. Amyloid protein-induced supramolecular self-assembly of water-soluble platinum(II) complexes: A luminescence assay for amyloid fibrillation detection and inhibitor screening. *J. Am. Chem. Soc.* **141**, 18570–18577 (2019).
47. Fan, D. Y. et al. Early intervention in Alzheimer's disease: How early is early enough? *Neurosci. Bull.* **36**, 195–197 (2020).
48. Liu, B. et al. Lanthanide functionalized metal-organic coordination polymer: Toward novel turn-on fluorescent sensing of amyloid β-peptide. *Anal. Chem.* **90**, 12449-12455 (2018).
49. Lei, L. et al. Glycopeptide nanofiber platform for Aβ-sialic acid interaction analysis and highly sensitive detection of Aβ. *Anal. Chem.* **91**, 8129–8136 (2019).
50. Kumar, M. et al. Monitoring early-stage protein aggregation by an aggregation-induced emission fluorogen. *Anal. Chem.* **89**, 9322-9329 (2017).
51. Yan, X. et al. *Endo*- and *exo*-functionalized tetraphenylethylene $M_{12}L_{24}$ nanospheres: Fluorescence emission inside a confined space. *J. Am. Chem. Soc.* **141**, 9673-9679 (2019).
52. Liu, H. et al. Small molecule-mediated co-assembly of amyloid β oligomers reduces neurotoxicity through promoting non-fibrillar aggregation. *Chem. Sci.* **11**, 7158–7169 (2020).

53. Liu, Y. et al. Highly specific noninvasive photoacoustic and positron emission tomography of brain plaque with functionalized croconium dye labeled by a radiotracer. *Chem. Sci.* **8**, 2710–2716 (2017).
54. Veloso, A. J. et al. Electrochemical immunosensors for effective evaluation of amyloid-*β* modulators on oligomeric and fibrillar aggregation process. *Anal. Chem.* **86**, 4901–4909 (2014).
55. Fu, H. et al. Highly sensitive near-infrared fluorophores for *in vivo* detection of amyloid-*β* plaques in Alzheimer's disease. *J. Med. Chem.* **58**, 6972–6983 (2015).
56. Zhao, D. S. et al. Exploring the binding mechanism of thioflavin-T to the *β*-amyloid peptide by blind docking method. *Sci. China Chem.* **55**, 112–117 (2011).
57. Yu, C. Y. Y. et al. A Photostable AIEgen for nucleolus and mitochondria imaging with organelle-specific emission. *J. Mater. Chem. B* **4**, 2614–2619 (2016**)**.
58. Donabedian, P. L. et al. Oligo (*p*-phenylene ethynylene) electrolytes: A novel molecular scaffold for optical tracking of amyloids. *ACS Chem. Neurosci.* **6**, 1526–1535 (2015).
59. Rahimi, F. et al. Photo-induced cross-linking of unmodified proteins (PICUP) applied to amyloidogenic peptides. *J. Vis. Exp.* **23**, e1071 (2009).
60. Frisch, M. J. et al. Gaussian 09, Revision A02, Gaussian, Inc., Wallingford CT, 2009.
61. Luhrs, T. et al. 3D structure of Alzheimer's amyloid-*β* (1–42) fibrils. *Proc. Natl. Acad. Sci. U.S.A.* **102**, 17342–17347 (2005).
62. Tomaselli, S. et al. The *α*-to-*β* conformational transition of Alzheimer's A*β*-(1-42) peptide in aqueous media is reversible: A step by step conformational analysis suggests the location of *β* conformation seeding. *ChemBioChem* **7**, 257–267 (2006).
63. RCSB protein data bank, http://www.rcsb.org/, Shanghai, China, 2021-01-14.
64. Michel, F. S. Python: A programming language for software integration and development. *J. Mol. Graphics Mod.* **17**, 57–61 (1999).
65. DeLano, W. L. 2008. *The PyMOL molecular graphics system*, Palo Alto, CA: DeLano Scientific LLC.

Figures

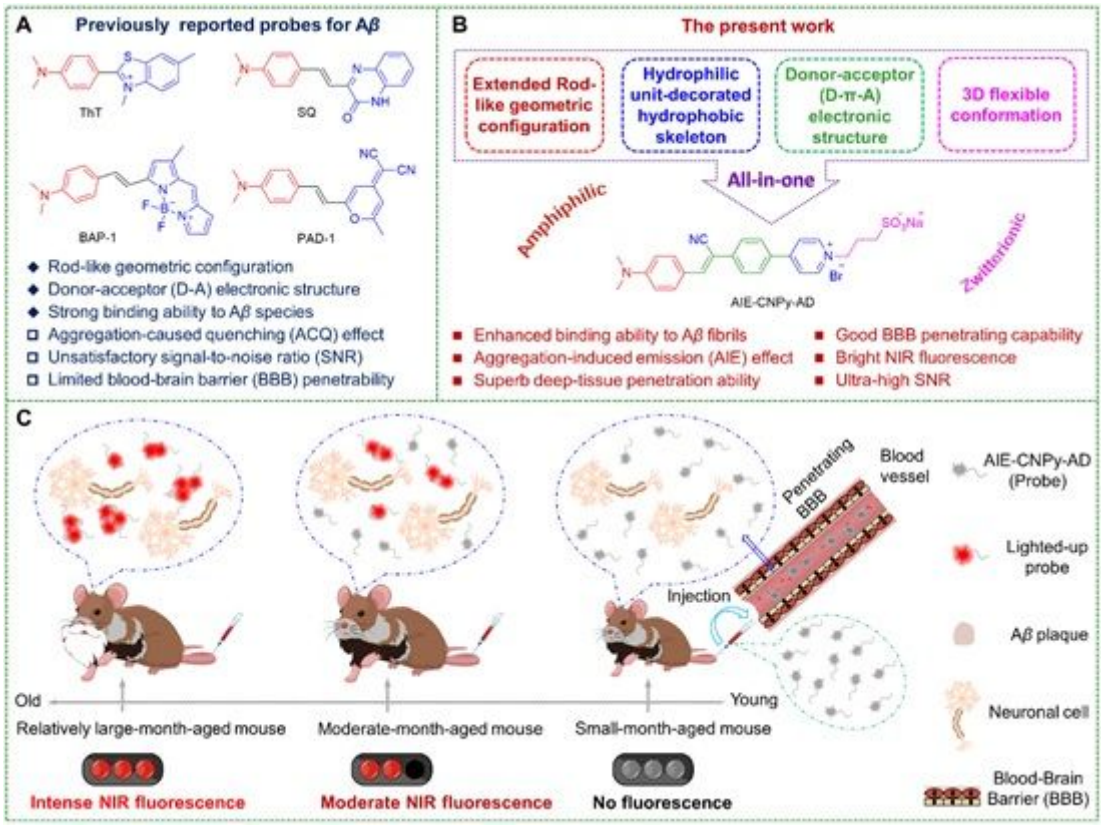

Figure 1

The “all-in-one” design principle. (A) Representatives of typical probes for Aβ detection with rod-like configuration and D-A electronic structure. (B) Our red/NIR AIE probe (AIE-CNPy-AD) for Aβ fibrils/plaques rationally constructed based on the proposed “all-in-one” design strategy. (C) Schematic illustration of the in-vivo imaging of Aβ plaques with AIE-CNPy-AD in brains of AD model mice in different age periods via tail vein injection, and the potential of AIE-CNPy-AD in early diagnosis of AD.

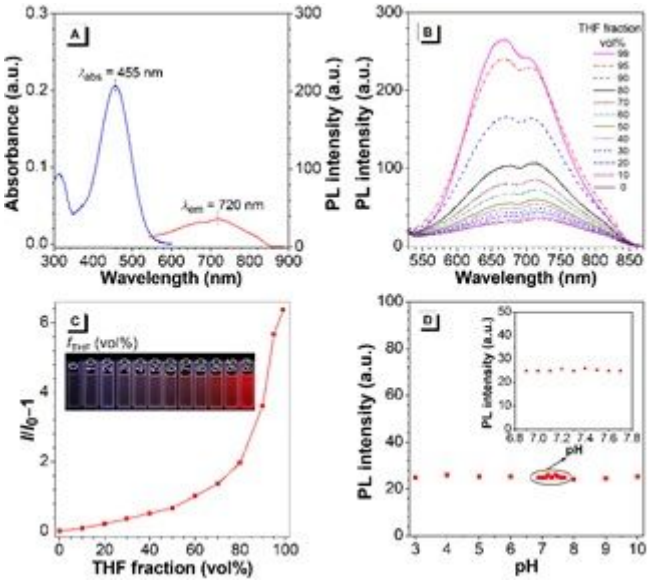

Figure 2

The photophysical properties of AIE-CNPy-AD. (A) Absorption (c = 10−5 M) and emission spectra (λex = 455 nm, c = 10−4 M) of AIE-CNPy-AD in the DMSO solution at room temperature. (B) Emission spectra of AIE-CNPy-AD in the DMSO/THF mixtures with different THF fractions at room temperature, λex = 455 nm, c = 10−5 M. (C) The plot of the emission enhancement (I/I0−1) versus the THF fractions. The inset: Corresponding fluorescent photographs of AIE-CNPy-AD in the DMSO/THF mixtures with different THF fractions taken under the irradiation at 365 nm with a handheld UV lamp. (D) The maximum fluorescence intensity of AIE-CNPy-AD which keeps unchanged under different pH values.

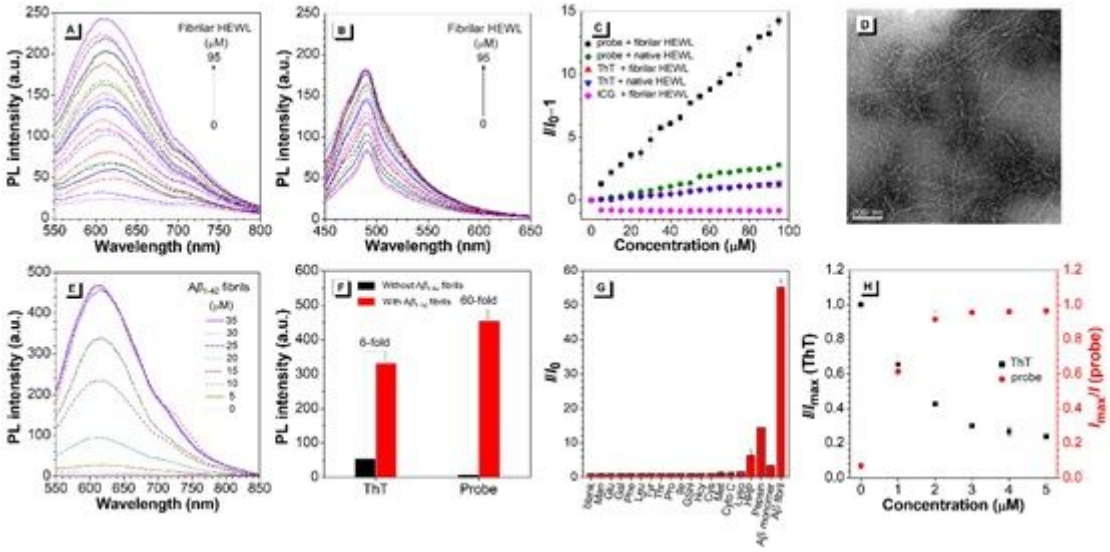

Figure 3

Evaluation on the specificity and affinity of AIE-CNPy-AD to Aβ fibrils. Emission spectra of (A) AIE-CNPy-AD (λex = 455 nm, c = 5 μM) and (B) ThT (λex = 420 nm, c = 5 μM) in PBS solution (pH = 7.4) with stepwise addition of fibrillar HEWL. (C) The plots of I/I01 of probe AIE-CNPy-AD, ThT and ICG versus different concentrations of fibrillar HEWL and native HEWL, c = 5 μM. (D) TEM images of pre-formed Aβ1−42 fibrils. (E) Emission spectra of AIE-CNPy-AD in PBS solution (pH = 7.4) with stepwise addition of Aβ1−42 fibrils, λex = 455 nm, c = 5 μM. (F) Fluorescence intensity of ThT and AIE-CNPy-AD bound with or without Aβ1−42 fibrils, respectively. (G) I/I0 response assay versus various analytes. (H) The plot of Imax/I of AIE-CNPy-AD and I/Imax of ThT versus different concentrations of AIE-CNPy-AD.

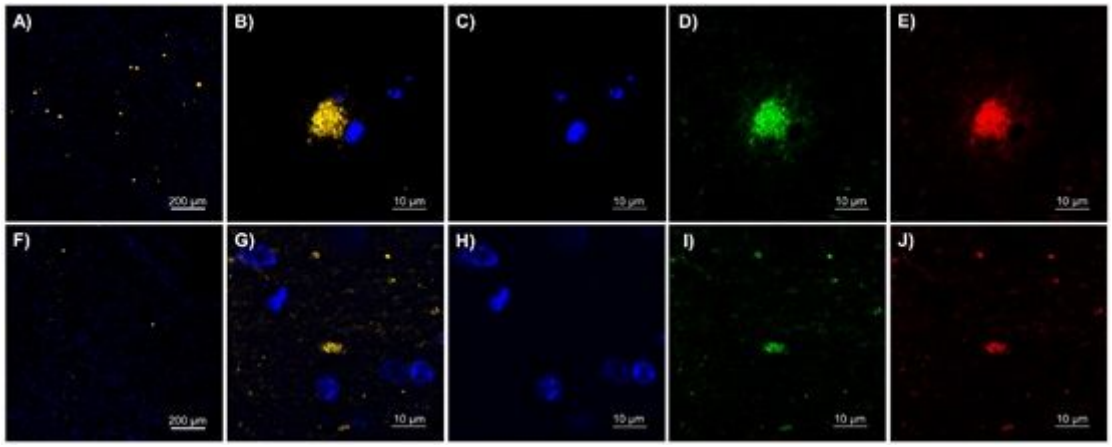

Figure 4

In-vitro fluorescent staining of paraffin slices of mice brains. Fluorescent staining of the brain slices of (A-E) 2.5-month-old 5*FAD transgenic mice and (F-J) 6-month-old APP/PS1 transgenic mice. The slices were co-stained with AIE-CNPy-AD, rabbit anti-mouse primary antibody (anti-beta amyloid 1-42 (mOC64), i.e., ab201060), Alexa Fluor® 488-labeled goat anti-rabbit secondary antibody (ab150077), and Hoechst 33342 in sequence. (A, B, F, G) Merged images of three channels; (C, H) Blue channel: Hoechst 33342, λex = 405 nm, λem = 461 nm; (D, I) Green channel: Alexa Fluor® 488, λex = 488 nm, λem = 519 nm; (E, J) Red channel: AIE-CNPy-AD, λex = 488 nm, λem = 620 nm. (A, F) 100× magnification, (B-E, G-J) 2000× magnification.

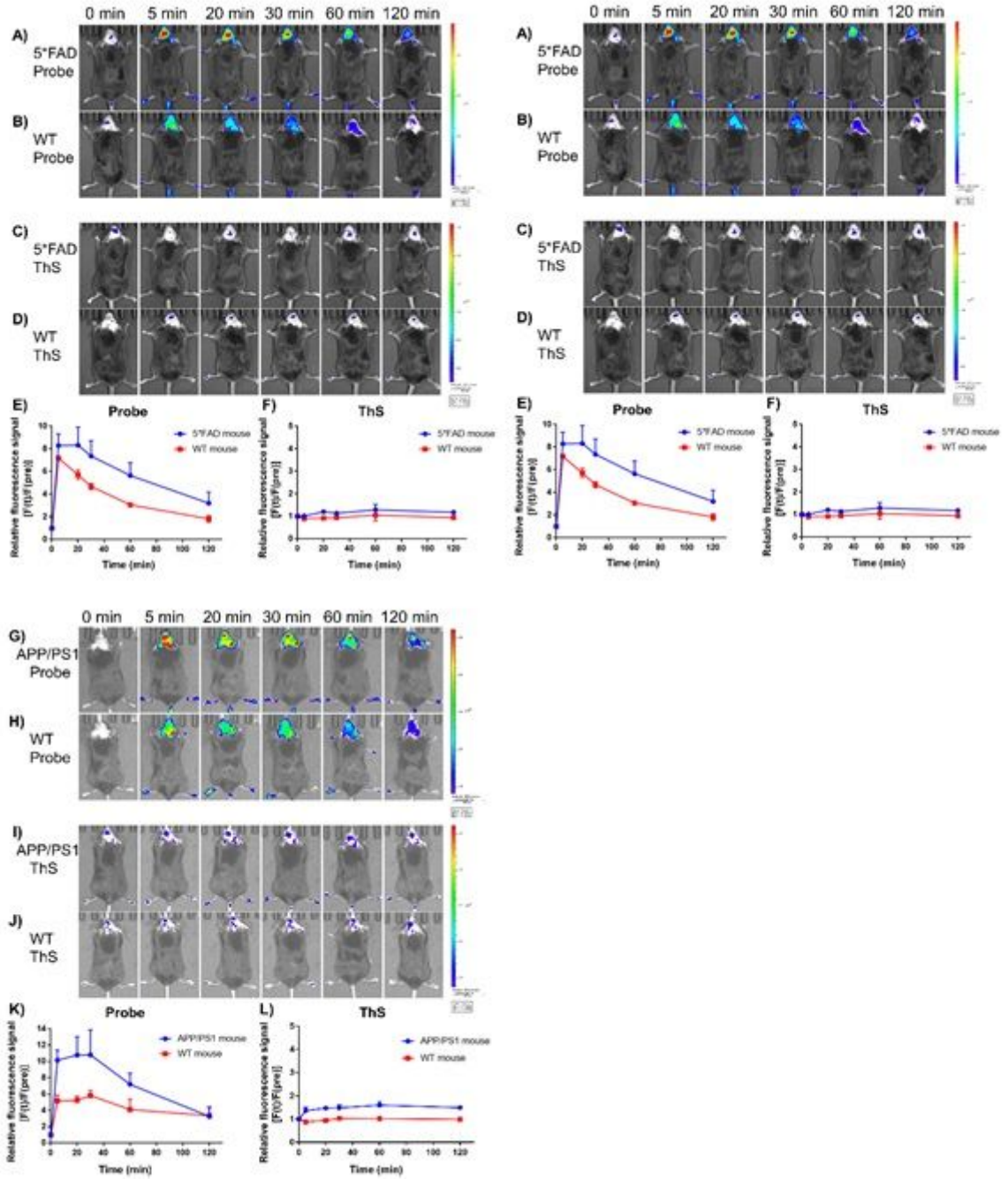

Figure 5

In-vivo imaging of Aβ plaques in live mice. Fluorescence images of (A) 5*FAD mice (2.5-month-old) and (B) wild-type mice (2.5-month-old) at different time points before and after via tail vein injection of AIE-CNPy-AD (2.0 mg/kg). Fluorescence images of (C) 5*FAD mice (2.5-month-old) and (D) wild-type mice (2.5-month-old) at different time points before and after via tail vein injection of ThS (2.0 mg/kg). The relative fluorescence signal [F(t)/F(pre)] in the brain regions of 5*FAD mice and wild-type mice after via tail vein injection of (E) AIE-CNPy-AD (2.0 mg/kg) or (F) ThS (2.0 mg/kg). Fluorescence images of (G) APP/PS1 mice (6-month-old) and (H) wild-type mice (6-month-old) at different time points before and after via tail vein injection of AIE-CNPy-AD (2.0 mg/kg). Fluorescence images of (I) APP/PS1 mice (6-month-old) and (J) wild-type mice (6-month-old) at different time points before and after via tail vein injection of ThS (2.0 mg/kg). The relative fluorescence signal [F(t)/F(pre)] in the brain regions of APP/PS1 mice and wild-type mice after via tail vein injection of (K) AIE-CNPy-AD (2.0 mg/kg) or (L) ThS (2.0 mg/kg). AIE-CNPy-AD: λex = 500 nm, λem = 620 nm; ThS: λex = 430 nm, λem = 500 nm.

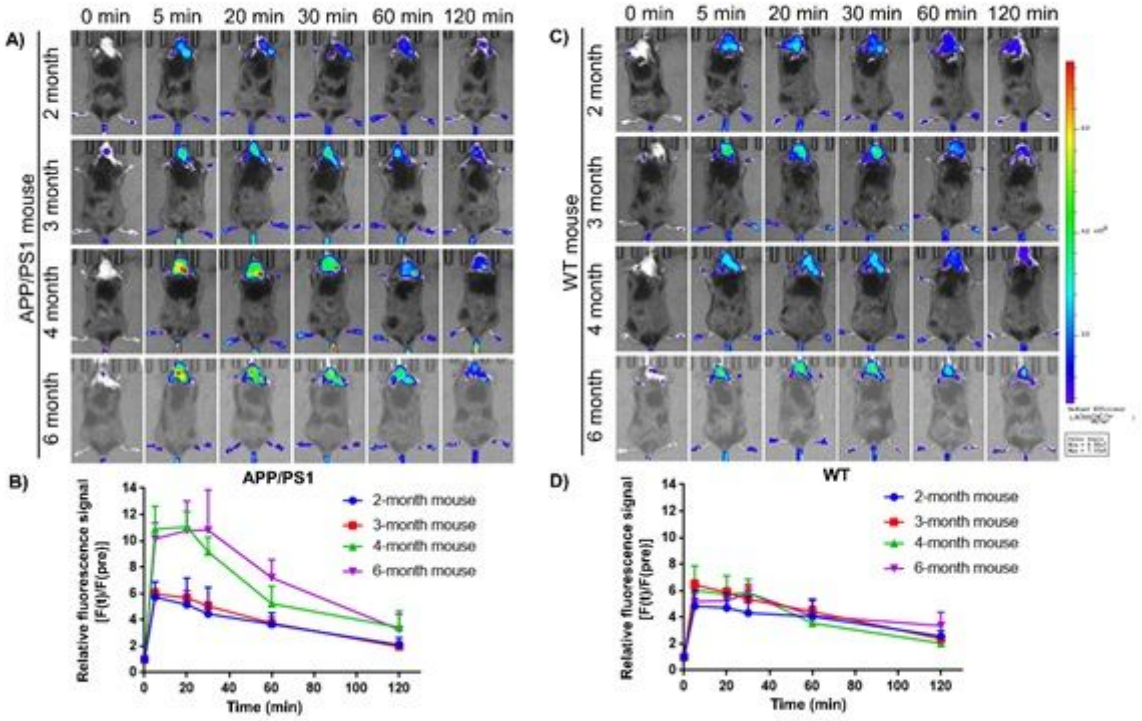

Figure 6

In-vivo tracking of Aβ plaques in APP/PS1 mice at different ages. Fluorescence images of (A) APP/PS1 mice or (C) wild-type mice of different ages (2-month-old, 3-month-old, 4-month-old, 6-month-old) at different time points taken before or at different time points after tail vein injection of AIE-CNPy-AD (2.0 mg/kg). The relative fluorescence signal [F(t)/F(pre)] in the brain regions of (B) APP/PS1 mice or (D) wild-type mice of different ages after via tail vein injection of AIE-CNPy-AD (2.0 mg/kg). AIE-CNPy-AD: λex = 500 nm, λem = 620 nm.

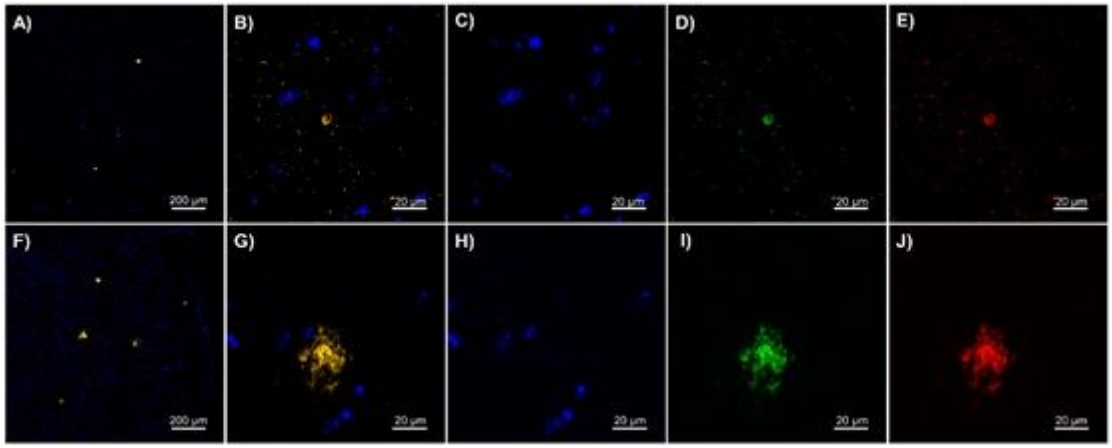

Figure 7

Ex-vivo observation of frozen brain slices of mice pre-administrated with AIE-CNPy-AD. Fluorescent staining of the brain slices of (A-E) 4-month-old APP/PS1 transgenic AD mice and (F-J) 6-month-old APP/PS1 transgenic AD mice. The slices of mice were pre-injected with AIE-CNPy-AD via tail vein injection, and then sequentially stained with anti-beta amyloid 1-42 (mOC64; ab201060) and Alexa Fluor® 488-labeled goat anti-rabbit secondary antibody (ab150077) after sacrificing. (A, B, F, G) Merged image of three channels; (C, H) Blue channel: Hoechst 33342, λex = 405 nm, λem = 461 nm; (D, I) Green channel: Alexa Fluor® 488-labeled antibody, λex = 488 nm, λem = 519 nm; (E, J) Red channel: AIE-CNPy-AD, λex = 488 nm, λem = 620 nm. (A, F) 100× magnification; (B-E, G-J) 1000× magnification.

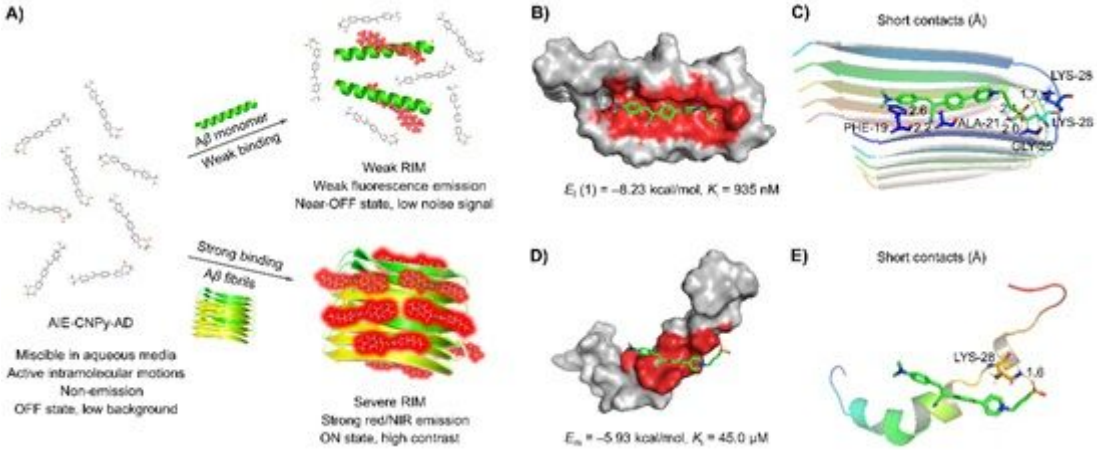

Figure 8

Working mechanism elucidated by molecular docking simulations. (A) Possible working mechanism of AIE-CNPy-AD in the specific detection of Aβ fibrils. The lowest energy binding mode of AIE-CNPy-AD with Aβ fibrils (PDB ID: 2BEG) in (B) surface representation52 and (C) cartoon representation. The lowest energy binding mode of AIE-CNPy-AD with Aβ monomer (PDB ID: 1Z0Q) in (D) surface representation and (E) cartoon representation. Ef: binding energy of AIE-CNPy-AD with Aβ fibrils; Em: binding energy of AIE-CNPy-AD with Aβ monomer. Ki is the inhibition constant.

Supplementary Files

This is a list of supplementary files associated with this preprint. Click to download.

- SupportingInformation.pdf